Detonation Performance of the CL-20-based Explosive LX-19

Carlos Chiquete*, and Scott I. Jackson

Shock and Detonation Physics Group
Los Alamos National Laboratory
Los Alamos, NM 87545 USA

Abstract

The generation of constitutive detonation performance model components for high explosives (HEs) invariably involves reference to experiment, as reliable first-principles determinations of these models are beyond our current capability. Whatever its form or complexity, the detonation performance model must be able to accurately capture the detonation wave timing and the energy release that it triggers upon arrival. Specifically, the HE products equation-of-state (EOS), which largely determines the detonating HE's ability to do useful work on its surroundings, is typically inferred from cylinder expansion tests where metal-confined HE cylinders are detonated and the ensuing outer confiner wall-expansion trajectory is recorded. Expensive, iterative comparisons to multimaterial hydrodynamic (or "hydrocode") simulations of these experiments are then used to constrain the parameters of the chosen EOS form. Here, we report on new detonation performance experiments produced for the highly-ideal, plastic-bonded explosive and CL-20-based LX-19 which are used to produce a new sub-scale detonation performance model for the explosive. This includes new products EOS and a new Detonation Shock Dynamics front propagation law. We also confirm the capability of two new, non-hydrocode-based products EOS generation techniques to accelerate the HE model parameterization process. This latter development is particularly significant for detonation performance modeling of new HE formulations.

Keywords: explosive, detonation, performance, cylinder expansion test, CL-20

*Corresponding author:
Email address: chiquete@lanl.gov (Carlos Chiquete)

1. Introduction

High explosives are metastable compounds that are commonly used in engineering applications that require extremely high power. The energetic molecule CL-20 or HNIW (2-4-6-8-10-12-Hexanitrohexaazaisowurtzitane) is one of the most energy dense explosives known to exist, with sensitivity similar to that of PETN [1]. Despite its potential, CL-20-based formulations are not commonly used for main-fill explosive applications involving detonation due in part to the limited detonation performance data available [1, 2]. It is however, specifically used in detonator design [3]. In this work, the detonation performance of the plastic-bonded explosive LX-19 is reported. Specifically, LX-19 is a plastic bonded explosive composed of (95.8% by weight percentage) CL-20 and plastic binder Estane (4.2%).

Detonation performance refers to the propagation speed of the detonation, how that speed varies with flow divergence or charge size, and the potential energy of the detonation products or their ability to do work on surrounding materials. Typically, the detonation velocity and its sensitivity to flow divergence is measured with a series of front-curvature "ratesticks" [4], which use a steady cylindrical geometry to relate the wave front shape and detonation velocity to finite-length reaction zone and flow divergence effects. The product energy and equation of state (EOS) is characterized using the detonation cylinder expansion test [5] (see Fig. 1), which yields the product isentrope from analysis of metal wall motion driven by the detonation products. The data from these tests is then used to calibrate a variety of models.

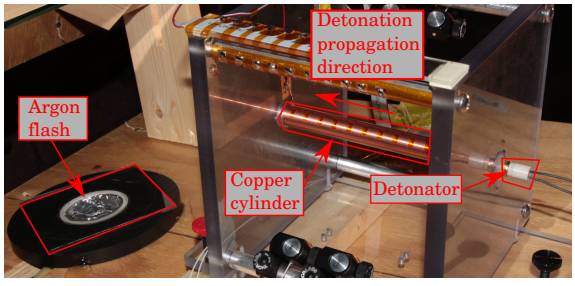

Figure 1: LX-19 CYLEX test 8-1885 (right) with argon flash (left). The red outlines highlight the labeled components.

Performance models must efficiently predict the wave propagation timing and energy delivery of high explosives (HEs) in large-scale geometries (with lengths on the order of a meter) while the detonation reaction zone length scales are typically five orders of magnitude smaller (on the order of 10 μm for ideal HEs like LX-19). Due to the disparity between these two scales, adequately resolving the detonation reaction zone still represents a significant computational challenge. Additionally, the underlying constitutive models and chemical kinetic pathways for these structurally and chemically complex energetic molecules are still being explored [6]. Reactive burn (RB) modeling approaches, which attempt to resolve the detonation reaction zone with an approximated reaction mechanism representing this complex chemistry, are intrinsically sensitive to numerical resolution and the multiscale nature of the engineering application complicates their use.

These issues therefore limit detailed multidimensional calculations and are addressed in practice with subscale modeling. Instead, Programmed burn (PB) models decouple the wave propagation from the subsequent energy delivery, thus avoiding the neccessity to resolve the reaction zone while still providing accurate timing information. Programmed burn methods therefore rely on subscale models for both wave propagation and energy release. The benefit of these approaches is that the calculations are significantly less sensitive to resolution and thus attractive in engineering applications due to the computational efficiency improvement relative to reactive flow or RB approaches. The RB and PB approaches do share some common elements, notably the products EOS which largely determines the energy delivery to the surrounding material. However, RB models additionally require a reaction rate model and reactant EOS, since the finite rate of reaction results in reactants coexisting with products in the reaction zone.

This work utilizes a PB methodology implemented in the multimaterial hydrodynamic (or "hydrocode") Flag [7, 8]. Detonation propagation is modeled with the Detonation Shock Dynamics (DSD) model [9, 10], which is able to predict the detonation velocity decrement from curvature that is induced by streamline divergence and finite-length reaction zone effects. The product EOS is modeled with the Jones-Wilkins-Lee (JWL) form [11, 12] and is aided by recent developments in product EOS prediction [13, 14], which are demonstrated to significantly optimize the process. This finding has significant consequences for calibration of new HE formulations.

Tarver et al [2] have previously produced a reactive flow model calibration for LX-19 relying on one-dimensional gas-gun experiments to generate shock Hugoniot data, initiating detonation profiles and a CYLEX test for the products. This data set is limited relative to other characterized explosives, as there is a

lack of diameter effect and associated front curvature data, limiting the range of validity of the model. Here, in contrast, our objective is to produce a sub-scale detonation performance model for the highly ideal LX-19 explosive that incorporates *multi-dimensional* propagation and energy release experiments. We first report on the calibration experiments, analyze the ratestick data via the generation of a new initial-density-sensitive DSD propagation law for detonation timing calculations, and then generate product EOS model from the single cylinder expansion test *without* direct reference to hydrocode simulations. Hydrocode analysis is then utilized to quantify the capability of these new methodologies for product EOS determination relative to the traditional method.

2. Experiments

Table 1: Summary of experimental tests where ρ_0 is the initial density, d_e is the charge-diameter, L refers to the ratetick length and D_0 is the detonation speed (with included experimental uncertainties).

Test No.	ρ_0 (g/cc)	d_e (mm)	L/d_e	D_0 (mm/μs)	Confiner
8-1881	1.942	6.4	25.2	9.190 ± 0.002	Air
8-1880	1.933	9.6	18.6	9.187 ± 0.008	Air
8-1883	1.881	12.7	12.0	8.987 ± 0.005	Air
8-1877	1.929	12.7	12.0	9.171 ± 0.004	Air
8-1872	1.930	25.0	12.3	9.189 ± 0.005	Air
8-1885	1.917	12.7	12.7	9.141 ± 0.003	Cu

Six experiments were fielded as summarized in Table 1. The front curvature ratesticks [4] were tested at four different diameters d_e of 6.4, 9.6, 12.7, and 25.0 mm. Two tests were fielded at the 12.7-mm or half-inch scale. Each ratestick was assembled from a number of explosive pellets of identical length and diameter as detailed in Table 1. The pellets were glued together with a low viscosity epoxy. Each ratestick was equipped with ionization wires to measure detonation velocity and an aluminized window to measure the front shape via the methods described in Ref. [4].

The cylinder expansion (CYLEX) test (Fig. 1) was 0.5-scale and consisted of a series of 12.7-mm-diameter pellets confined by a copper tube with an inner diameter of 12.8 mm, an outer diameter of 15.3 mm, and a length of 152 mm. The tube was oxygen-free high thermal conductivity (OFHC) C101 copper that was annealed dead soft. Pellets were bonded with Sylgard 184 elastomer, which was also used to fill any voids between the pellets and the tube wall to prevent jetting. The cylinder expansion test was instrumented with ionization wires, an aluminized window on the detonation breakout face, and four PDV probes to record the wall expansion velocity.

All tests were directly initiated by an RP-1 or RP-2 exploding bridge wire detonator from Teledyne RISI. The LX-19 pellets fabricated by uniaxially ram pressing LX-19 molding powder into dies of the final diameter. Pressing was performed with three individual presses (with some amount of dwell time included in between) at a pressure of 414 MPa (60 kpsi) and die temperatures ranging from 50–100°C. Normally it is preferable to to machine performance explosive parts from an isostatically pressed billet to avoid local density variations associated with uniaxial ram pressing, but insufficient LX-19 molding powder was available for this method. The magnitude of this variation was not diagnosed for each individual part used in this study but it is likely to be small in comparison to the evident part-to-part variation. Final pellet densities were measured with an immersion densitometer. In the experiments, pellets were ordered with increasing density from the initiation end. The LX-19 molding powder was formulated by ATK Aerospace Systems with care taken to ensure that the CL-20 was in the epsilon (ϵ) phase.

Detonation velocities D_0 for each experiment were determined from a linear fit to to the trigger time versus positions of the ionization wires. The resulting velocities are listed in Table 1 along with associated standard errors and these are also plotted in Fig. 2 (top) versus inverse charge-radius. Detonation front shapes are also shown in Fig. 2 (bottom) as a function of r (the distance from the charge center).

3. HE model components

3.1. Detonation Shock Dynamics calibration

The DSD propagation law relates the normal detonation velocity (D_n) to its local surface curvature (κ), and is typically calibrated via the ratestick tests which produce steady-state detonation propagation. Here, the functional form that represents this law has a cubic dependence on curvature,

$$D_n(\kappa) = D_{CJ}(1 - B\kappa(1 + C\kappa^2)) \quad (1)$$

where D_{CJ}, B and C are the propagation law parameters. The Chapman-Jouguet (CJ) speed D_{CJ} is the unsupported planar wave speed for the explosive. The initial HE density ρ_0 can vary in practice and has a significant effect on D_0. Thus, the $D_n(\kappa)$ functional parameters

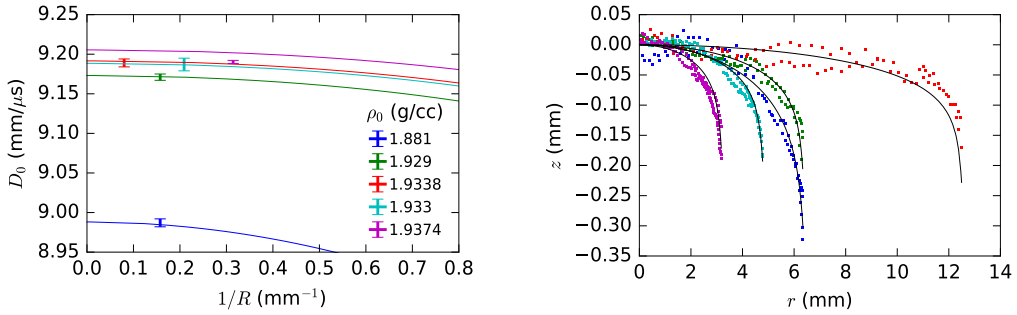

Figure 2: Comparison of diameter effect and front shape data (symbols) to the DSD calculations (black curves). Experimental uncertainties in the phase velocities are indicated by the error bars (left).

contain a linear density-dependent correction to represent this sensitivity,

$$D_{CJ} = D_{CJ,n} + \beta_1(\rho_0 - \rho_{0,n}), \quad (2)$$

$$B = B_n + \beta_2(\rho_0 - \rho_{0,n}),\ C = C_n + \beta_3(\rho_0 - \rho_{0,n}) \quad (3)$$

where the subscript "n" refers to each parameter's nominal value at the nominal initial density $\rho_{0,n}$. There is a notion from Hill & Aslam [15] that B should increase with ρ_0 (encoded in their similar linear dependency for D_{CJ} and B), given its interpretation as a measure of the reaction zone length and and that increasing density is associated with diminished hotspot formation and therefore bulk reaction strength. Nevertheless, the main rationale for the specific linear forms used here is based on their utility in fitting the available data. The calibration procedure then depends on optimizing $D_{CJ,n}$, B_n, C_n and β_i for $i = 1, 2$ and 3. Additionally, there is an edge angle parameter (ϕ) that represents the interaction with the surrounding material (air) and due to its weakness, this value is equivalent to the sonic edge angle, ϕ_s. Jackson & Short [4] detail how steady-state phase velocities and front shapes are calculated from a given $D_n(\kappa)$ law.

Table 2: The initial-density-sensitive $D_n(\kappa)$ law parameters obtained from numerical optimization of comparison to front shapes and phase velocities.

$\rho_{0,n}$ (g/cm^3)	$D_{CJ,n}$ (mm/μs)	B_n (mm)	C_n (mm^2)	ϕ_s (deg.)
1.933	9.1885	0.01980	0.165	35.4
β_1 (mm/μs/g/cm^3)	β_2 (mm/g/cm^3)	β_3 ((mm/g/cm^3)^2)		
3.85321	-0.32430	0.01836		

The DSD parameters were obtained by minimization of a merit function incorporating the differences in phase velocity and front shapes between DSD calculations and data,

$$\mathcal{M} = W_{DE} \sum_{i=1}^{N_{DE}} \frac{1}{N_{DE}} [(D_{0,i}^{DSD} - D_{0,i}^{exp})/D_{0,i}^{exp}]^2 + W_{FS} \sum_{i=1}^{N_{DE}} \frac{1}{N_{FS,i}} \sum_{j}^{N_{FS,i}} [(z_{ij}^{DSD} - z_{ij}^{exp})/R_i^{exp}]^2 \quad (4)$$

where W_{DE} and W_{FS} balance the contribution to the overall error metric of each type of error (diameter effect vs. front shape), N_{DE} is the number of diameter effect points, $D_{0,i}^{exp}$ is the experimentally measured detonation speed, $D_{0,i}^{DSD}$ is the corresponding DSD calculation, $N_{FS,i}$ is the number of front shape points for each test, z_{ij}^{DSD} is the DSD calculation of the front shape at the j-th radial coordinate within the i-th experimental data set, z_{ij}^{exp} is the corresponding experimental measurement of the front shape, and R_i^{exp} is the charge-radius. For $W_{FS} = 100.0$ and $W_{DE} = 1.0$, the numerical minimization (via [16]) of this error function produces the parameters in Table 2 and the comparison of DSD calculations to data seen in Fig. 2. The fit represents the phase velocity and front shape data data well, at a RMS error level of 5.4 m/s and 16.6 μm, respectively. The model performance is very good, specially given the broad range of initial densities represented in the calibration data set.

3.2. Products equation-of-states

The JWL form [11, 12] was used to represent the products EOS for the HE. This incomplete EOS relates pressure to its internal energy and specific volume according to the Mie-Grüneisen form, $p(v, e) = p_s(v) + (\omega/v)(e - e_s(v))$, where $v = 1/\rho$ and the pressure and internal energy reference functions are specific to the isentrope (i.e. $de_s/dv = -p_s$). Substitution of the

specific JWL isentrope reference functions leads to

$$p(v,e) = A\Big(1-\frac{\omega v_0}{R_1 v}\Big)\exp\Big(-\frac{R_1 v}{v_0}\Big)+ B\Big(1-\frac{\omega v_0}{R_2 v}\Big)\exp\Big(-\frac{R_2 v}{v_0}\Big)+\frac{\omega}{v}(e-e_0), \quad (5)$$

where A, B, R_1, R_2 and ω are the model parameters and e_0 is a constant of integration such that $p(v_0, 0) = 0$ (standard convention in condensed-phase detonation where the ambient pressure is negligible relative to the post-shock values). This particular form will help define our subscale energy release model in section 4.

Typically, hydrocode simulations of the previously described cylinder expansion test are used to constrain the parameters of the model equation of state in (5) via a time-consuming iterative process. Jackson has recently described two separate methods [13, 14] to either generate a products EOS from experimental data without hydrocode modeling or to provide good initial parameter estimates that can reduce the number of hydrocode iterations necessary to achieve a good fit. Here, we generate JWL parameters from these methods and compare them to previously obtained JWL for the explosive [2]. In the following section, these parameter values will be refined via hydrocode optimization to assess their capability for the present data set.

The first approach [14] takes advantage of a product EOS scaling relationship that is able to predict a JWL using only the experimental ρ_0 and D_0 as inputs. The second [13] derives the product EOS p from the cylinder wall acceleration (by differentiating the fitted wall velocity) and produce v from the cylinder expansion (integrating the wall velocity). The JWL parameters derived from applying each method to test 8-1885 are listed in Table 3 and plotted in Figure 3 along with the hydrocode-derived JWL from Tarver et al [2]. Graphically, the JWLs overlay well despite the large spread of parameter values. In part, this is due to the non-uniqueness of the JWL form. The wall-motion analytic fit does appear to be slightly lower in pressure and less energetic than the other JWLs. The consequences of these seemingly small differences will be explored in the context of hydrocode CYLEX simulations in the following.

4. Hydrocode simulations and calibration

In this section, the CYLEX data is fit using hydrocode modeling and the effectiveness of the prior JWL generation methods is analyzed. In the following, we specify the essential elements of this simulation and parameterization process.

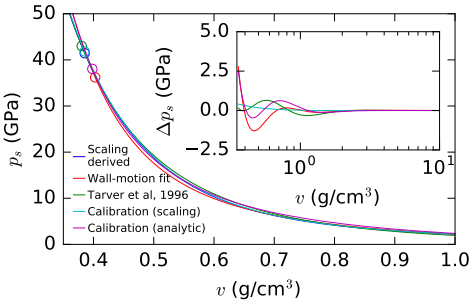

Figure 3: Relevant products EOS isentropes for scaled, wall-motion derived, a previously identified JWL for LX-19[2] and two new hydrocode-based calibrations. The open circles represent the CJ state pressure and specific volume obtained from each model. Inset shows absolute differences between the models relative to the scaling-derived result.

Table 3: a) JWL parameters from empirical scaling relationship [14], b) wall motion analytical fit [13], c) refers to hydrocode fitting in Ref. [2], d) calibration result that used the scaling correlation result as a starting point and e) calibration result from the analytic reduction case. The fidelity of each model to the wall motion data is represented by the error functional evaluation of $\mathcal{M}$ in (8).

	A (GPa)	B (GPa)	R_1	R_2	ω	E_{det} ($\frac{mm^2}{\mu s^2}$)	v_0 ($\frac{cm^3}{g}$)	$\mathcal{M}$ (m/s)
a	905.6	19.7	4.52	1.36	0.3043	6.3184	0.5216	25.1
b	2826.3	66.3	6.46	1.98	0.3000	6.3230	0.5225	56.9
c	1637.9	186.3	6.50	2.70	0.5500	5.9217	0.5149	46.4
d	911.7	20.3	4.52	1.36	0.3043	6.2987	0.5216	23.8
e	2605.9	76.5	6.46	1.98	0.3000	6.3922	0.5225	25.1

4.1. Governing equations

The compressible Euler equations are used to model the post-shock flow evolution,

$$\frac{D\rho}{Dt}+\rho\nabla\cdot\mathbf{u}=0,\ \frac{D\mathbf{u}}{Dt}=-\frac{1}{\rho}\nabla p,\ \frac{De}{Dt}=\frac{p}{\rho^2}\frac{D\rho}{Dt} \quad (6)$$

where $D/Dt = \partial/\partial t + \mathbf{u}\cdot\nabla$ is the material derivative, t is time, ρ, $\mathbf{u}$, e and p are the density, material velocity vector, specific internal energy and pressure, respectively. The simulations were performed in the multi-physics, multimaterial Lagrangian hydrodynamics code Flag [7, 8].

4.2. Detonation performance sub-scale HE model

The detonation performance is modeled with an established approach known as velocity-adjusted Jones-Wilkins-Lee (VAJWL). The version of this method we

use is slightly different from a previous description in [17] (we note specifically how below). As in other PB approaches, the detonation propagation information for VAJWL is first produced in a pre-processing step. In this case, this is done via DSD, as implemented in our target hydrocode which follows [18]. Therein, a level set field ψ is evolved according to $\partial\psi/\partial t + D_n(\kappa)|\nabla\psi| = 0$, where $\psi = 0$ represents the location of the detonation front, $D_n(\kappa)$ is defined by (1) with parameters as defined in the previous section. The solution of the mixed parabolic-hyperbolic level-set equation also requires a boundary condition where the shape of the front at HE-confiner interfaces is set through the specification of the edge angle parameter ϕ. This value enables different strengths of confinement to affect the wave shape and velocity. The shock normal edge angle to characterize the LX-19/copper pair was 20.0° as derived from fitting the experimentally measured front shape for ϕ_e (given the previously determined $D_n(\kappa)$). This calculation provides two key quantities needed in the hydrodynamic phase of the calculation, the time-of-arrival field of the detonation front at every point $\mathbf{x}$ in the HE geometry $t_b(\mathbf{x})$ and the local detonation front normal velocity $D_n(\mathbf{x})$ which gauges the wave curvature effect imposed by the geometry and confiner on the detonation flow.

The second component of the detonation performance model is the energy release. The VAJWL approach scales the energy release with the local shock strength to avoid the numerical issues that arise when these quantities are not in sync. This would occur here if the same (planar) energy release profile was prescribed across the curved front, regardless of the reduced shock strength predicted by DSD. To achieve the reduced pressure jump across the shock in the hydro, the closure relation in (5) that gives pressure as function of the internal energy and density obtained from the hydrodynamics is modified according to

$$p(v,e) = \tilde{A}(D_n)\Big(1 - \frac{\omega v_0}{\tilde{R}_1(D_n)v}\Big)\exp\Big(-\frac{\tilde{R}_1(D_n)v}{v_0}\Big) + B\Big(1 - \frac{\omega v_0}{R_2 v}\Big)\exp\Big(-\frac{R_2 v}{v_0}\Big) + \frac{\omega}{v}(e - e_0 + \lambda E_{det}), \quad (7)$$

where λ refers to the pre-programmed reaction progress, E_{det} is the detonation energy, and $\tilde{A}$ and $\tilde{R}_1$ are generalized JWL parameters which now depend on the localized shock strength D_n felt by a particular fluid particle at an initial location $\mathbf{x}$. Two major consequences for the hydrodynamics are imposed in (7), firstly, as λ is only activated when the shock has passed through a particular fluid particle location, ($\lambda = 0, t < t_b(\mathbf{x})$ or $\lambda = 1, t > t_b(\mathbf{x})$), the energy offset due to detonation is applied instantaneously and only occurs at the pre-programmed time and initial location. Also, crucially,

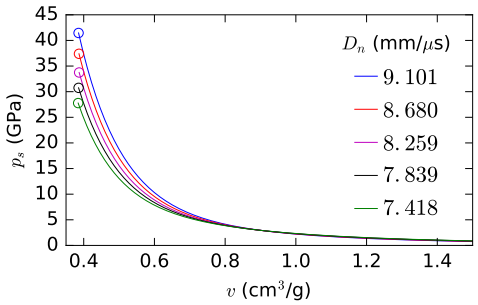

Figure 4: Modified products isentropes such that "CJ speed" is made equal to a given normal shock speed $D_n < D_{CJ}$. This is achieved via fitting of A and R_1 products EOS parameters. Note the decreasing initial pressure state that results from the incorporation of the reduced shock speed relative to the 1D CJ case (in blue).

the EOS parameters $R_1 \rightarrow \tilde{R}_1(D_n)$ and $A \rightarrow \tilde{A}(D_n)$ are modified, element by element, such that given the pressure jump experienced by a given fluid particle is now dependent on the shock strength (a feature missing in the case where wave curvature effect is ignored or $D_n = D_{CJ}$). The main reasoning for choosing these two specific parameters for modification is that it modifies the products EOS isentrope mainly at higher pressures, keeping the trajectory largely the same at lower pressures. This is achieved by enforcing that the modified $\tilde{A}$ and $\tilde{R}_1$ generate a lower CJ velocity for that fluid element that is equal to the local D_n (without modifying E_{det}). The end result of this process is that post-shock, the pressure jump is then reduced (as shown in Fig. 4) and the energy delivered to the confiner is placed on a different trajectory relative to the planar or CJ case. This approach differs with [17] in the two adjusted parameters, specifically they use A and B.

4.3. Products EOS calibration

A major motivation of employing the JWL generation methods of [13, 14] is to provide a credible starting point for the more expensive hydrocode-based calibration of the products EOS, thus reducing the needed iterations to arrive at a satisfactory result. In the best case scenario, the non-hydrocode based products EOSs produce a sufficiently close correspondence to the data in the hydrocode simulation context that no iterations are needed at all. Whether these outcomes are achieved is investigated below.

The hydrocode simulations output the wall motion profiles at the outer copper surface at various axial lo-

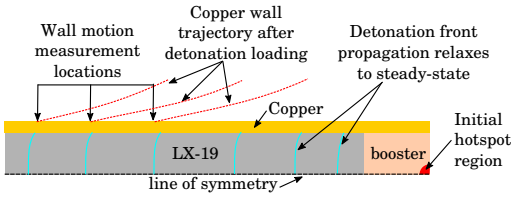

Figure 5: Schematic of the CYLEX simulation geometry.

cations, to confirm the necessary relaxation to steady-state for a meaningful comparison to the experimental data (see schematic Fig. 5). To complete the material models needed in the calculations, the confining copper material was modeled using a tabular equation-of-state detailed in [19] and its plastic deformation under shock loading from the HE was modeled according to the model described in [20]. These specific material models and basic numerical methodologies have been previously validated to experiment [21, 22]. The error function incorporating this comparison that was numerically minimized to produce the optimal EOS parameters was simply the mean of the root-mean-square errors for the 4 measurements of the wall velocity ($\mathbf{v}_{expt}^{probe}$) with respect to the calculated post-shock wall motion velocity ($\mathbf{v}_{calc}$),

$$\mathcal{M} = \sum_{probe=1}^{4} RMS(\mathbf{v}_{data}^{probe} - \mathbf{v}_{calc})/4 \qquad (8)$$

where $RMS(\mathbf{x}) = (\sum_i^N \mathbf{x}_i^2/N)^{1/2}$. Only two parameters were selected for optimization, i.e. the pressure amplitudes represented by A and B in (7). Modification of these two parameters ensured we were able to modify both the high and low pressure regimes in each iteration and therefore find sufficient quality fits based on just these two parameters. We also note that including more parameters did not materially modify the overall fit quality due primarily to the good initial guesses for the majority of the parameters provided by the cited approximate methodologies. Also, at each iteration, the detonation energy parameter E_{det} was modified to ensure the CJ speed was consistent between the products JWL and the DSD propagation law. The numerical algorithm chosen to obtain the merit function minimum was a sequential least squares method which provides a parameter bounding feature [23]. After a convergence study for the wall motion profile, a resolution of 125 μm was selected to calibrate the EOS. This resolution provided a good balance of computational speed and also was able represent the characteristic ringing evident in the wall motion traces as the transmitted shock reverberates in the copper (see Fig. 7). Snapshots of the p profile in the HE which drives the copper motion appear in Fig. 6 and the ρ field in the copper is also shown to illustrate the origin of this feature.

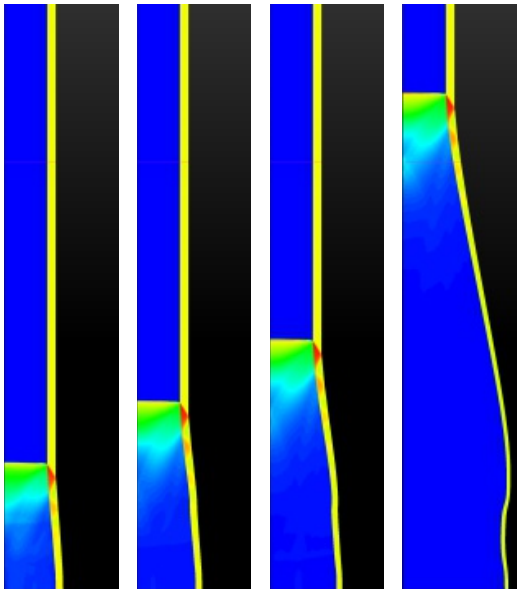

Figure 6: Snapshots of the early and late-time HE and copper flow evolution for the scaling correlation JWL derived model.

4.4. Comparing the models

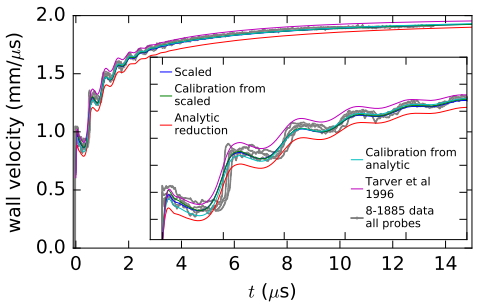

Figure 7: Comparison of calculated wall motion profiles for the various products EOS models to the experimental data. Inset is focused on early time post-jump behavior.

Figure 7 shows the wall motion profiles for the three EOSs from Table 3 and two hydrocode-optimized results which originated from the scaled and analytic reduction parameter sets (all using the same DSD law). The hydrocode-optimized parameters appear in Table

3d-e. There are a number of interesting observations to highlight: Firstly, the scaling-derived EOS [14] provides a very good correspondence to the experiment capturing the late time saturation process as well. As a result, the iterations that follow from this initial starting point do not greatly modify the comparison to the data. Secondly, the analytic result [13] is slightly underpowered in the drive imparted into the copper. The subsequent iterations, in this case, do appreciably change the correspondence to the data. Within 10 iterations however, the correspondence to that data generates similar error values with respect to the scaling derived results (see Table 3 for a direct comparison of the models via this metric). It is also interesting to note that the two calibrated model wall motion results overlay but greatly differ in their parameter values, particularly in the R_1 and R_2 exponential parameters. This suggests that the JWL functional form parameters are not constrained by the experimental trace – whether this is a due to the repeated exponential basis function is not clear. Other starting points were attempted for the numerical minimization procedure and it was found that similar quality solutions were not necessarily obtained with progress stalling at higher error levels. For reference, we used the previously determined products JWL by Tarver et al [2] and find that it is predictably too energetic relative to the available data as it was based on higher initial density experiments – emphasizing the need to recalibrate for significant departures in initial density.

Finally, as a point of reference, Zocher et al [22] modeled PBX 9501 (another highly ideal explosive) using a reactive burn approach and simulated the wall motion of a CYLEX test. The differences between model and experiment developed here compare favorably to those shown in [22] though, they do not give specific error value for quantitative comparison. Additionally, the present error level was found to be comparable to Mortensen and Souers [24] who also calibrated a JWL EOS using a programmed burn methodology for a highly idealized HE. Importantly, these authors similarly find that a resolution of 125 μm ensures a converged result.

5. Conclusions

This work has reported on recent performance experiments for LX-19, a powerful CL-20-based conventional or highly-ideal HE. These data were used to parameterize a sub-scale detonation performance model which used Detonations Shock Dynamics to generate detonation front shape and velocity and a velocity-adjusted JWL product EOS for energy release (which is sensitive to finite-reaction zone effects). Two new products EOS generation techniques were used to significantly accelerate the generation of hydrocode-informed EOSs. One was based on analytic reduction analysis of the cylinder wall motion and the other was based on a products EOS scaling relationship. While both produced good parameter estimates for the subsequent hydrocode-based optimization process, the initial JWL prediction from the scaling method stood out in its close correspondence to experiment. Whether this persists for other explosives is to be determined.

References

References

[1] R. Simpson, P. Urtiew, D. Ornellas, G. Moody, K. Scribner, D. Hoffman, CL-20 performance exceeds that of HMX and its sensitivity is moderate, Prop. Expl. Pyro. 22 (1997) 249–255.

[2] C. M. Tarver, R. L. Simpson, P. A. Urtiew, in: AIP Conference Proceedings, volume 370, AIP, pp. 891–894.

[3] J. D. Olles, R. R. Wixom, R. Knepper, J. P. Ball, M. B. Ritchey, T. Reedy, Characterizing the initiation performance of CL-20 based detonators, Technical Report SAND2017-4726C, Sandia National Laboratory, 2017.

[4] S. I. Jackson, M. Short, Scaling of detonation velocity in cylinder and slab geometries for ideal, insensitive and non-ideal explosives, J. Fluid Mech. 773 (2015) 224–266.

[5] E. Lee, H. Horning, J. Kury, Adiabatic expansion of high explosives detonation products, Technical Report TID 4500-UCRL 50422, Lawrence Livermore National Laboratory, 1968.

[6] R. W. Molt, R. J. Bartlett, T. Watson, A. P. Bazanté, Conformers of CL-20 Explosive and ab Initio Refinement Using Perturbation Theory: Implications to Detonation Mechanisms, J. Phys. Chem. A 116 (2012) 12129–12135.

[7] E. J. Caramana, D. E. Burton, M. J. Shashkov, P. P. Whalen, The construction of compatible hydrodynamics algorithms utilizing conservation of total energy, J. Comp. Phys. 146 (1998) 227–262.

[8] D. E. Burton, Multidimensional discretization of conservation laws for unstructured polyhedral grids, Technical Report UCRL-JC-118306, Lawrence Livermore National Laboratory, 1994.

[9] J. B. Bdzil, D. S. Stewart, Modeling two-dimensional detonations with detonation shock dynamics, Phys. Fluids A: Fluid Dyn. 1 (1989) 1261.

[10] J. B. Bdzil, W. Fickett, D. S. Stewart, in: Proc. 9th Intl. Symp. on Detonation, pp. 730–42.

[11] B. Dobratz, Properties of chemical explosives and explosive simulants, Technical Report UCRL-5319, Lawrence Livermore National Laboratory, 1972.

[12] E. Lee, M. Finger, W. Collins, JWL equation of state coefficients for high explosives, Technical Report UCID-16189, Lawrence Livermore National Laboratory, 1973.

[13] S. I. Jackson, An analytic method for two-dimensional wall motion and product isentrope from the detonation cylinder test, Proc. Combust. Inst. 35 (2015) 1997–2004.

[14] S. I. Jackson, Scaling of the detonation product state with reactant kinetic energy, Combust. Flame 190 (2018) 240–251.

[15] L. G. Hill, T. D. Aslam, in: Proc. 11th Intl. Symp. on Detonation, pp. 730–42.

[16] J. A. Nelder, R. Mead, A simplex method for function minimization, Comput. J. 7 (1965) 308–313.

[17] D. C. Hetherington, N. J. Whitworth, in: AIP Conference Proceedings, volume 1426, AIP, pp. 259–262.
[18] T. D. Aslam, J. B. Bdzil, D. S. Stewart, Level set methods applied to modeling detonation shock dynamics, J. Comput. Phys. 126 (1996) 390–409.
[19] J. H. Peterson, K. G. Honnell, C. Greeff, J. D. Johnson, J. Boettger, S. Crockett, in: AIP Conference Proceedings, volume 1426, AIP, pp. 763–766.
[20] D. L. Preston, D. L. Tonks, D. C. Wallace, Model of plastic deformation for extreme loading conditions, J. Appl. Phys. 93 (2003) 211–220.
[21] H. O. Wooten, V. H. Whitley, Analysis of historical and recent PBX 9404 cylinder tests using FLAG, Technical Report LA-UR-16-24389, Los Alamos National Laboratory, 2016.
[22] M. A. Zocher, T. D. Aslam, S. I. Jackson, E. K. Anderson, in: Proc. 16th Intl. Symp. on Detonation.
[23] D. Kraft, A software package for sequential quadratic programming, Technical Report DFVLR-FB 88-28, DLR German Aerospace Center – Institute for Flight Mechanics, 1988.
[24] C. Mortensen, P. C. Souers, Optimizing Code Calibration of the JWL Explosive Equation-of-State to the Cylinder Test, Prop. Expl. Pyro. 42 (2017) 616–622.